RSC Advances

Accepted Manuscript

RSC Publishing

www.rsc.org/advances
Registered Charity Number 207890

Boron-rich ordered mesoporous carbon from solvent-evaporation-induced self-assembly with tailorable microstructure and excellent electrochemical capacitance

Xiaochen Zhao, Qiang Zhang, Bingsen Zhang, Cheng-Meng Chen, Jinming Xu, Aiqin Wang, Dang Sheng Su, Tao Zhang

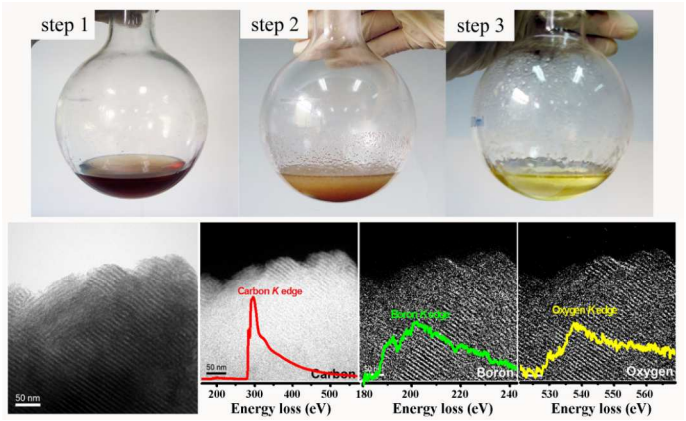

The boron-rich ordered mesoporous carbons were formed via a solvent evaporation-induced self-assembly strategy with controllable boron incorporation, tailorable microstructure, and extraordinary electrochemical capacitance.

View Article Online

Cite this: DOI: 10.1039/c0xx00000x

www.rsc.org/xxxxxx

PAPER

Decorated resol derived mesoporous carbon: highly ordered microstructure, rich boron incorporation, and excellent electrochemical capacitance

Xiaochen Zhao,[a,e] Qiang Zhang,[b] Bingsen Zhang,[c] Cheng-Meng Chen,[d] Jinming Xu,[a,e] Aiqin Wang,[a] Dang Sheng Su,[*c] Tao Zhang [*a]

Received (in XXX, XXX) Xth XXXXXXXXX 20XX, Accepted Xth XXXXXXXXX 20XX
DOI: 10.1039/b000000x

Nanoarchitecturing of carbon with assembled building blocks in diverse scales with superior physical properties and tunable chemical characters is of great importance for energy storage. Therefore, exploring boron-modified ordered mesoporous carbons (OMCs) with tailorable microstructure and controllable incorporation become scientifically necessary. In this contribution, the boron-rich ordered mesoporous carbons were formed via a solvent evaporation-induced self-assembly strategy with controllable boron incorporation, tailorable microstructure, and extraordinary electrochemical capacitance. The incorporated boron content can be verified from 0 to 1.64 wt%, and the obtained B-OMCs exhibited widened potential window and enhanced specific capacitance. A maximum value of B incorporation (1.01~1.35 wt%) was detected in improving the specific capacitance (0.38~0.39 Fm^{-2}). This is attributed to the specific oxygen chemisorption and the strengthen surface polarization accompanied with B modification. These results demonstrate the material chemistry, widen the potential applications, and in consequence allow mechanistic insight into the roles boron played for OMC textures and electrochemical activities.

1. Introduction

Nanoarchitecturing of carbon with assembled building blocks in diverse scales is of great importance for energy storage.[1] Besides the common feature of porous carbon materials, ordered mesoporous carbons (OMCs) are further improved by periodically arranged uniform mesopore space, tailorable pore sizes, and alternative pore shapes.[2] Therefore, OMC has been widely explored for promising applications in energy conversion, adsorption, drug delivery, and heterogeneous catalysis.[3] However, the diverse applications of OMCs are not only bonded to their superior physical properties, such as meso-structural associated parameters, electric and thermal conductivity, but also to their chemical characters.

In OMCs, the termination of nanocarbon sheets is intrinsically decorated by abundant active sites, such as lattice defects and functional groups. Thus the chemical properties of OMC can be tailored by heteroatom functionalization on graphene or molecular carbon geometries at the edges, defects, or strained regions etc. Hitherto, great effort has been made to develop heteroatom (such as B,[4-8] N,[6,9,10] O,[8] P,[7,9,11] S[12, 13]) incorporated OMCs and the results show that the electronic properties of carbon can be mediated and hence render greatly improved catalytic activities and electrochemical performances. Therefore, heteroatom incorporated OMCs have been regarded as advanced electrode materials in electrochemical energy storage[5,7,14] and metal-free catalysts for oxygen reduction reaction (in fuel cell),[10] triglyceride transesterification (in biomass conversion),[13] as well as oxidative dehydrogenation and alkane activation reactions.[15]

Among various heteroatoms involved in OMC, boron is a unique element, bearing three valence electrons. When boron is doped in carbon lattice as electron acceptor, a shift in the Fermi level to the conducting band is presented, indicating a modified electronic structure. The boron-doped carbon hence exhibited superior capacitance as advanced electrode materials.[5,14] Besides, when boron is incorporated into the carbon framework, series of redox reactions can be carried out due to a catalytic effect of oxygen chemisorption on the modified carbon surface.[16]

Taking into account of both porous structure and surface chemistry, few successful attempts were reported in the fabrication of boron-rich OMCs while maintaining a similar structural system as the B-free one, albeit widely investigated.[4-8] Thus, exploring boron-modified OMC with tailorable microstructure and controllable incorporation is scientifically necessary to demonstrate the material chemistry, widen the potential applications, and in consequence allow mechanistic insight into the roles boron played for their textures and activities.

Generally, the formation of boron-modified OMC requires boron/carbon source as the precursor and hard/soft templates as the mesopore-forming agents. Herein, the boron-rich OMCs were

fabricated via a solvent-evaporation-induced self-assembly (EISA) method, which allowing efficient synthesis of OMCs with controllable multi-level pore structures.[17] The as-obtained boron-rich OMCs were with controllable boron incorporation, tailorable microstructure, and extraordinary electrochemical capacitance.

2. Results and discussion

In the current EISA strategy, B-modified resol was pre-synthesized, and following by a self-assembly with tri-copolymer F127 and a further curing process, the obtained soluble resol ultimately transformed into B-decorated, well ordered mesoporous polymer. After a carbonization at 800 °C in N_2 atmosphere, consequent B-modified OMCs were fabricated and donated as Bx-OMC, in which x represented the ratio of boric acid to phenol. The key point of our synthesis is the elegant functionalization of resols with B via oxygen bridges. This can be realized by intermolecular dehydration of boric acid and water-free monomethylol phenols, as shown in Fig. 1 and Fig. S1. At beginning, boric acid is unsolvable or semisoluble in water free monomethylol phenols. However, after the mixture of boric acid and water-free monomethylol reacted at the temperature of 120°C for several minutes, the turbid mixture turned transparent, indicating that the boric acid was dissolved and reacted with the monomethylol, forming homogeneous B-modified resol. In contrast with physically mixed precursors,[5,7] the resultant B-modified precursor played a role of both boron and carbon sources. This not only simplified the following organic–organic assembly process, provided tailorable mesoporous structure, but also helped to enhance the introduction of B to the resultant carbon materials, comparison details were listed in Table S1.

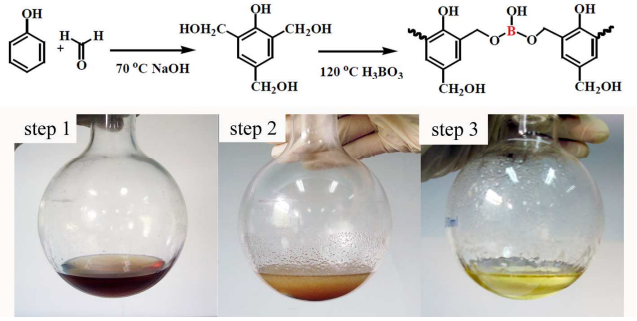

Fig. 1 The proposed synthesis scheme of B-modified resol and photographs of current synthesis process: *step 1* showed the water-free monomethylol phenols, *step 2* showed the mixture of boric acid and water-free monomethylol phenols, *step 3* showed the pre-polymerized B-modified resol after dehydration at the temperature of 120 °C.

To investigate the introduction and distribution of B element in the resultant modified-OMCs, electron energy loss spectroscopy (EELS), energy filtered TEM (EFTEM), and high-angle annular dark-field (HAADF) - scanning transmission electron microscopy (STEM), and energy-dispersive X-ray spectroscopy (EDS) mapping were conducted on B0.3-OMC. According to Fig. 2a and 2b, the EELS predicted a simultaneous presence of C, O and B elements, while the mapping images employed under EFTEM mode confirmed that B and O functionalities were homogeneously distributed in the carbonaceous framework. Besides, since no specific procedure was carried out to get rid of the involved salt species, sodium was also supposed to exist in the resultant materials. However, the Na element is hard to detect by EELS because the elemental edge is at high-energy region. However, the Na can be confirmed by the EDS spectra (Fig. 2c). The HAADF-STEM image, C, O, Na maps, and the spectra provide an unambiguous evidence for the uniform distribution of O, C, as well as Na species in B0.3-OMC. Combined with the EELS and EDS mapping, it is well confirmed that the B, C, O, Na were homogeneously distributed in the B0.3-OMC matrix.

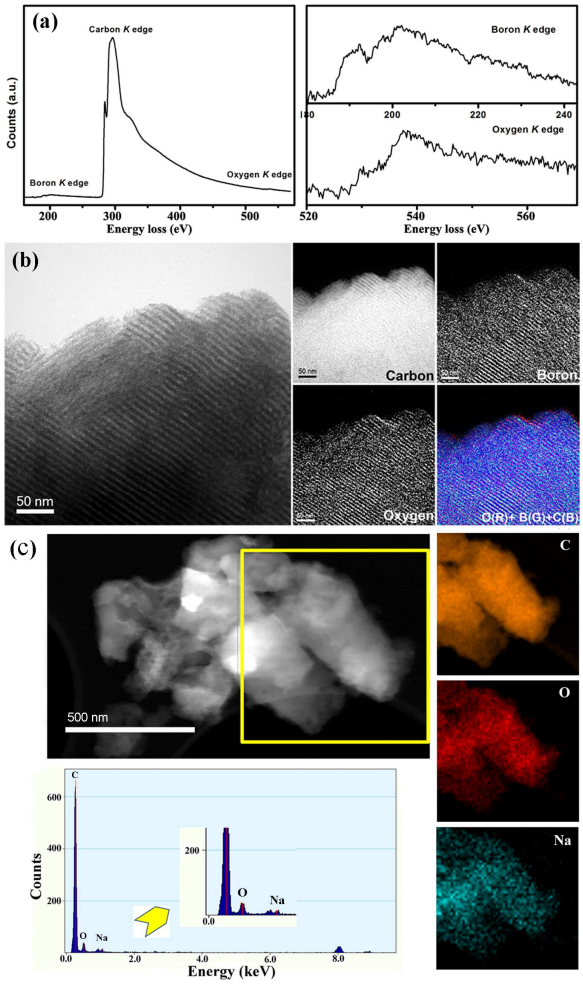

Fig. 2 (a) EELS, (b) EFTEM: zero loss image, C, B, O energy filtered images and their colored combination, (c) HAADF-STEM image, C, O, Na maps, and EDS spectra of B0.3-OMC.

To designate and compare the actual functionalities of B-modified OMC, X-ray photoelectron spectroscopy (XPS) was further employed on B-free OMC and B0.3-OMC. The results were listed in Fig. 3, S2, and Table 1. The O1s spectra demonstrated characteristic features of carbon materials, while B1s spectra revealed that B was introduced in the carbon materials mainly in the form of oxygen-containing species.[5,7] Besides, in the sample of B0.3-OMC, the survey of XPS and Na1s fine scanning spectra (Fig. S1) also indicate the existence of sodium salts, [18] which origined from the neutralization of basic catalyst with acidic boron functionalities.

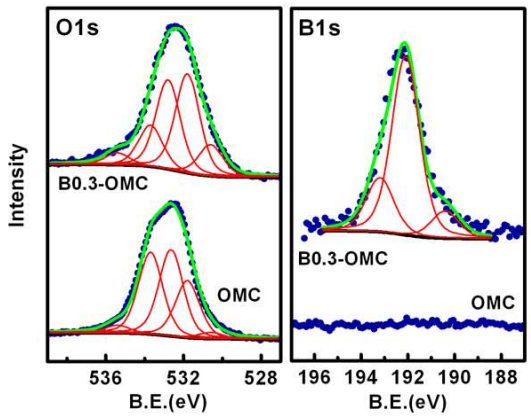

Fig. 3 O1s and B1s XPS spectra of B0.3-OMC. The dark blue dots are raw densities, the red lines are fitted species and the green solid curves are summed densities.

Table 1 XPS results of B0.3-OMC and OMC samples.

Element	B.E. (eV)	Content (wt%)	
		OMC	B0.3-OMC
O	530.6 (Quinone)	0.31	1.53
	531.8 (C=O)	2.88	4.82
	532.8 (C-O)	4.36	4.34
	533.7 (C-OH)	4.14	2.01
	535.4 (H_2O adsorb.)	0.39	0.59
	Total content	12.08	13.29
B	190.4 (BC_2O)	--	0.16
	192.1 (BCO_2)	--	1.04
	193.2 (B_2O_3)	--	0.32
	Total content	--	1.52

According to the proportion of oxygen species calculated in Table 1, it can be concluded that the B introduction increases the overall oxygen content compared with B-free OMC. Particularly, the ratio of quinines and carbonyl oxygen in esters or anhydrides increased drastically after B modification from 0.31 to 1.43 wt% and 2.88 to 4.51 wt%, respectively. This is ascribed to the inhibited pyrolysis process after B introduction,[19] leaving more thermal stable quinines and carbonyl groups in the as-obtained materials. On the contrary, the content of carboxyl oxygen in B-OMC decreased from 4.14 to 1.88 wt% due to the consumption of carboxyl groups when dehydrated with boric acid.

Preparation of heteroatom bearing precursor was considered as an *in-situ* modification strategy, thus the introduction of B influenced not only the resultant materials but also their pyrolysis performance. In the XRD patterns (Fig. 4a) of B-OMCs, series of new peaks appeared when x increased to 0.6, the tiny one at around 20.3°, marked with *, can be assigned as macromolecular compounds (reference code: 00-053-1867). This suggested again that B introduction hampered the pyrolysis process and thus resulted incompletely carbonized materials, in consistent with previous reports[19] and TGA analysis (Fig. S3). Moreover, over addition of boric acid also induced large amounts of unreacted boric acid remaining in the system (details shown in Fig. S1), taking part in self-assembly process, and hence being trapped in the composite matrix. During pyrolysis and carbonization, most of the overdosed dissociated B sources were forced to get rid of the carbon materials along with the N_2 flow, but inevitably left some B species transformed into B_2O_3 and detected in the samples of B0.6-OMC and B1.0-OMC, marked with Δ (reference code: 00-006-0297). Besides, it is worth noting that the boric acid adding amount is not actually the concentration that incorporated in B-OMCs. Because the modified precursor suffers a drastic pyrolysis process, during which lots of oxygen functionalities, as well as B functionalities, were get rid of the carbon structures.

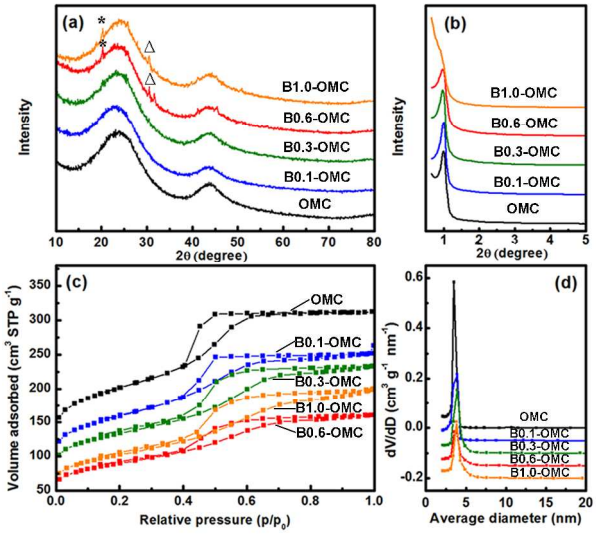

Fig. 4 (a) Routine XRD patterns, (b) low-angle XRD patterns, (c) N_2 sorption isotherms and (d) BJH pore size distributions of Bx-OMCs.

Table 2 Structural parameters, B contents and Specific capacitance of EISA-B modified OMC

Sam-ple	S_{BET} m^2/g	S_{micro} m^2/g	V_p m^3/g	V_{micro} cm^3/g	D_p nm	a_0[a] nm	$B_{cont.}$[b] wt%	C[c] F/m^2
OMC	694	343	0.48	0.16	3.4	10.3	--	0.19
B0.1	551	250	0.41	0.12	3.6	10.3	0.67	0.29
B0.3	462	212	0.36	0.10	3.7	10.5	1.01	0.38
B0.6	314	120	0.25	0.05	3.7	10.5	1.35	0.39
B1.0	357	133	0.31	0.06	3.8	10.6	1.64	0.35

[a] a_0 is the cell parameter calculated as $a_0 = 2\times d_{(100)}/\sqrt{3}$.

[b] determined by ICP

[c] Specific capacitance of per surface area.

Since heteroatom incorporation was reported to suppress framework shrinkage during pyrolysis,[7] the cell parameters (a_0) of B-OMCs were calculated according to low angle XRD patterns. As shown in Fig. 4b and Table 2, the increasing value of a_0 after modification indicated that B element was successfully incorporated in the matrix of B-OMCs; in another aspect, the

barely variation of a_0 and well preserved structural ordering as a function of B content can be attributed to the elegant modified resol with B-O species. Thanks to the short bond length of B-O (1.28-1.43 Å),[20] which influences little on textual parameters, the meso-structural orderings were well preserved even when B content increase to 1.64 wt%, as shown in Fig. 4b and Fig. 5d. Fig. 4b shows the low-angle XRD patterns of B-OMCs, and the strong peaks of B-OMCs centred at around $2\theta = 1.0^{o}$ can be indexed as the (100) reflection of 2D hexagonal ordered mesostructures. Although ordered structures were obtained, it is obvious that the (100) peaks were gradually widened along with the increase of B content, suggesting that large amount of B introduction may induce a deterioration of the long range structural order. This was ascribed to the overdose of unreacted boric acid, as shown in Fig. S1 and S3, which may not only interfer the self-assembly process but also inhibit the cross-linking and condensation of carbon precursors.

Meanwhile, the N_2 sorption isotherms (Fig. 4c) describe typical IV type isotherms with H1 hysterises loops. This type of isotherms depict characteristic of mesoporous structure, while the reduced adsorption volumes at high P/P_0 indicate B as a negative function of both surface area and pore volume. The pore size distributions were demonstrated in Fig. 4d and all structural parameters were summarized in Table 2. It is obvious that the BET surface area, microporous area, total volume, and microporous volume all decrease as the content of B increase. Since most of the micropores in chemical derived carbons are origined from the release of small molecular gases during pyrolysis, the lack of surface area and volume in B-OMC samples is attributed to the well preservation of quinine and carbonyl groups, which, on the other hand, sacrifices the formation of micropores.

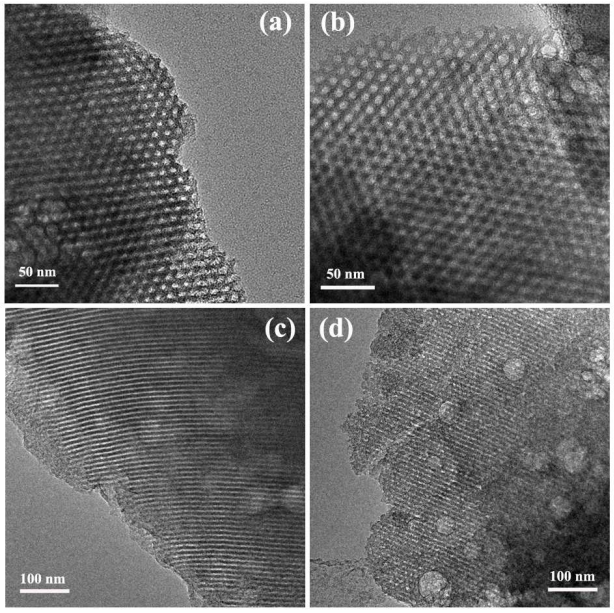

Fig. 5 TEM images of (a) B0.1-OMC, (b) B0.3-OMC, (c) B0.6-OMC, and (d) B1.0-OMC.

The TEM images in Fig. 5 pictured well ordered mesoporous structure of the obtained B-OMCs, while their directly estimated cell parameters were consistent with that calculated by low-angle XRD patterns. Combined with TEM images in large scales (Fig. S4), it can be observed that besides ordered mesopores, spherical macropores were also generated in B-OMCs. Intuitively shown in Fig. S1, increasing boric acid addition may result in more unreacted B in the system, due to the thermodynamic equilibrium of the dehydration reaction (in Fig 1). These dissociated B species were consequently trapped in the matrix of nanocomposites and finally formed macropores in the as-synthesized carbon matrix during carbonization process. These new generated macropores are also speculated to be responsible for the decrease of pore volumes as a function of B content.

Supercapacitors, which are contributed by electrical double layer capacitance and pseudo-capacitance, are promising power sources for complementing rechargable batteries in portable electronics, power management, and hybrid electric vehicles because of their large power density and longer cycle-life.[21] In order to evaluate the capacitor performance of Bx-OMCs, the as-prepared materials were characterized by cyclic voltammetry (CV) (Fig. 6a) and Galvanostat charge-discharge (GC) (Fig. 6b) profiles. The caculated capacitance revealed a general increase tendency when B was firstly introduced. Nevertheless, when the value of x is over 0.3 in Bx-OMC, sharp reductions of gravemetric capacitance occurred due to the related decrease of surface area. To rule out the influence of structrual properties, Fig. 6c demonstrated the normalized specific capacitances of B-OMCs as a function of B content with a scan rate of 2 $mV{\cdot}s^{-1}$, which was supposed to reflect the intrinsic charge storage function per unit area. A drastic increase of specific capacitance was observed when B concentration is below 1.35 wt%, however, more B introduction led to a decrease rather than further improvement of specific capacitance. This indicated a maximum value of B introduction for interfacial capacitance enhancement. Correlated the capacitor performance with the surface functionalites, the increase of quinine and carbonyl groups along with B introduction contributes to the pseudofaradic charge transfer on oxygen groups,[22] as shown in Fig. 7a. On the other hand, the presence of B via oxygen bridge may increase the polarization of medium under an applied electric field, therefore enhance the resultant capacitance likewise.

Besides the overall enlargment of specific capacitance, the shape of CV cures scanning at 2 mV/s (Fig. 6a) also changed after B-modification. During the charging process, inhibition of electrolyte decomposition was observed on all the B-OMCs, indicating a widened potential window and a consequent higher energy density. This can be well explained by an enhanced oxidation resistance acquired after B-modification,[23] which subsequently results in a blockage of electrolyte decomposition. Cosistent with phosphorus enriched carbon which was exploited in acidic conditions and realized a widend potential window, our results further examplified a similar possibility of B in basic solution.[24] Nevertheless, in alkaline solution, hydroxyl ion is oxidized, more or less, into water and oxygen at high positive potential. Some of these nascent oxygens release from the system, others are adsorbed on the surface of nanopores due to the driving force of the negative polarization. In the case of B-OMCs, oxygen-containing B functionalities were assumed to enhance the storage of *in situ* produced oxygen. When employing negative

potentials, bulge curves were obtained in B-OMCs below the potential of -0.2 V, which are supposed to correspond to the electro-reduction of sorbed oxygen. Thus, in addition to the electrical double-layer capacitor storage and pseudofaradic reaction on oxygen groups, the capacity origined from the enhanced oxygen adorption also contribute to the total charge.

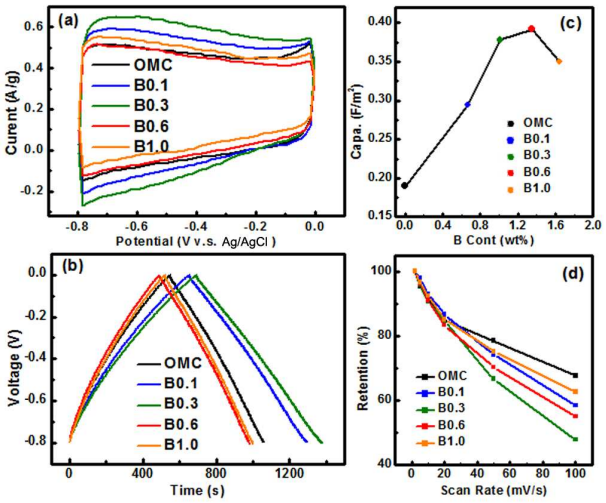

Fig. 6 (a) CV curves of Bx-OMCs at a scan rate of 2 mV/s, (b) GC curves of Bx-OMCs at a scan rate of 0.2 A/g, (c) Specific capacitance as a function of B content and (d) Capacitance retention as a function of potential scan rate in a 6.0 M KOH electrolyte.

However, at the expense of enhanced pseudocapacitance, more response time was required for the faradic reaction. Meanwhile, due to the variation of conductivity and surface hydrophilicity accompanied with B incorporation, the kinetic hindrance was also strengthened in the transport of both electrons and electrolyte ions. To demonstrate this point, we conducted CV tests at different scan rates (Fig. 6d). Compared with B-free OMC, B modification caused inferior retention ratio in general. However, as B content increase, this inferiority aggravated at first, whereafter exhibited an improved tendency in the case of B0.6-OMC and B1.0-OMC. Combined with structual analysis, low B incorporation influenced little on porosities, thus, the variation of retention is mainly controlled by the kinetic rather than the diffuse limitation. Nevertheless, large amount of B modification induced drastic decreases in micro-pore volume and, meanwhile, generated a large amount of macropores. As a result, the diffusion of electrolyte ions is benifited by these structual modulations, which overcomes the negative function of conductivity and kinetic hindrance induced by B incorporation, and hence resulted in a rise up of retention ratio at high scan rate.

3. Conclusions

2D ordered B-incorporated OMCs, which are promising electrode materials for supercapacitors, have been successfully fabricated by an EISA method. The incorporated boron content can be verified from 0 to 1.64 wt.%, while maintaining the well ordered structure of mesoporous carbon. The obtained B-OMCs exhibited widened potential window and enhanced specific capacitance, which are essential parameters for energy and power density, respectively. Moreover, a maximum value of B incorporation (1.01~1.35 wt.%) were detected in improving the specific capacitance (0.38~0.39 $F \cdot m^{-2}$). The superior performance of B-OMC can be attributed to the specific oxygen chemisorption, the strengthen surface polarization and the enhanced hydrogen adorption accompanied with B modification. Although the optimization of surface area is beyond the scope of this work, further augmentation of available surface area of the obtained B-OMCs by conventional activations is highly desired in practical applications to realize ultra superior capacitance in future.

4. Experimental

4.1 Synthesis procedure for heteroatoms-doped ordered mesoporous carbons

A low-molecular-weight soluble phenolic resin was prepared by mixing 21.0 g phenol, 22.0 g formaldehyde (37 wt%) and 3.75 g of 20 wt% sodium hydroxide (NaOH) aqueous solution together in a flask at the temperature of 50 °C. The temperature was gradually increased to 75 °C and the stirring was maintained for 1.0 h. After the mixture was cooled down to room temperature, the water in reaction system was removed by vacuum evaporation below 50 °C. Then 1.25 g of boric acid was added to the water free mixture and kept stirring for another 5.0 min. The obtained mixture was put into a pre-heated oil bath and followed by a further stirring of 0.5 h at the temperature of 120 °C, while new generated water was removed again by employing vacuum evaporation. The final product was dissolved in ethanol with the help of ultrasonic equipment and then was diluted to a concentration of 30 wt%. The obtained modified resol was donated as B0.1-R, in which 0.1 represented the ratio of boric acid to phenol.

B0.1-OMC was synthesized by a solvent evaporation induced self-assembly method. In a typical preparation, 3.0 g F127 were dissolved in 20.0 g ethanol in the presence of 0.3 g HCl (37 wt%). Then 10.0 g diluted B0.1-R (30 wt%) was added drop wise and kept stirring for 0.5 h. The homogeneous solution was poured into dishes to evaporate ethanol at room temperature for overnight, followed by heating in oven at 100 °C for 24 h. The well cured transparent films were scraped and then heated under a N_2 atmosphere at 350 °C for 2.0 h to remove the surfactant and followed by carbonization at 800 °C for 2.0 h, at a ramping rate of 1.0 °C min^{-1}. The final product is denoted as B0.1-OMC.

By varying the amount of boric acid addition, B-OMCs with different B concentrations were fabricated and donated as Bx-OMC, with x represented the atomic ratio of boric acid to phenol.

4.2 Characterizations

Nitrogen adsorption–desorption measurements were performed at -196 °C with a Micromeritics ASAP2010 instrument. Prior to the measurements, the samples were degassed at 110 °C for 1.0 h and at 250 °C for 3.0 h. The specific surface areas were calculated with BET equation and the average pore diameters were estimated with desorption branches based on Bopp, Jancsó, and Heinzinger (BJH) model.

XRD patterns were collected on a PW3040/60 X' Pert PRO (PANalytical) diffractometer equipped with a Cu K_α radiation source (λ = 0.15432 nm), operating at 40 kV, 40 mA for wide angle and 40 kV, 30 mA for low angle, respectively. A continuous mode was used for collecting data in the 2θ range from 10 ° to 80 ° for wide angle and from 0.5 ° to 4.5 ° for low angle.

TEM images were obtained on a Philips CM200 LaB_6 microscope operating at 200 kV, and EELS spectrum and energy-filtered images were obtained on a FEI Cs-corrected Titan 80-300 microscope operating at 80.0 kV. The HAADF-STEM, and EDS mapping were carried out on a FEI Tecnai G2 F20 microscope operating at 200 kV. The sample was ultrasonically dispersed in ethanol, and then a drop of the solution was deposited on a holey C/Cu TEM grid to be used for TEM, STEM and EELS characterization.

XPS was conducted on ESCALAB250 (Thermo VG Corporation) equipped with a Al K_α radiation (1486.6 eV, 15 kV, 10 mA, 150W). All binding energies were calibrated with graphitic carbon C1s peak at BE of 284.5 eV as a reference. The recorded spectra were fitted by a least square procedure to a product of Gaussian-Lorentzian functions after subtraction of background noise. The concentration of each element was calculated from the area of the corresponding peak calibrated with the atomic sensitivity factor.

4. 3 Electrochemical measurements

For preparing a working electrode, a mixture of an active material, carbon black and poly(tetrafluoroethylene) with a weight ratio of 90:5:5 was ground together to form a homogeneous slurry. The slurry was squeezed into a film and then punched into pellets with a surface area of 1.0 cm^2 for each piece. The punched pellets with a nickel foam on each side was pressed under 6.0 MPa for 1.0 min and dried overnight at 120 °C. Prior to the electrochemical tests, the electrodes were impregnated with electrolyte under vacuum for several hours. The CV tests were conducted using Zahner Elektrik IM6e electrochemical workstation in a three-electrode cell system, in which a sintered $Ni(OH)_2$/NiOOH as the counter electrode, a Ag/AgCl as the reference electrode and a 6.0 M KOH solution as the electrolyte. A scan rate of 2, 5, 10, 20, 50, and 100 mV s^{-1} was applied respectively in the CV studies. The GC measurement was conducted on automatic LAND battery test instrument (CT2001A) to elvaluate the charge/discharge performance and a current of 0.2 A g^{-1} current was applied in GC studies.

The specific capacitance of a single electrode (C_{elec}) was calculated from the CV curves based on the equation,

$$C_{elec} = idt/dv$$

where *i* is the instant current in Amperes per gram of active material and *dv/dt is* the scanning rate in Volts per second.

The specific capacitance of the cell (C_{cell}) was calculated from GC profiles based on the following equation,

$$C_{cell} = (I\Delta t)/\Delta U$$

where I is the discharge current in Amperes per gram of active material, Δt is the discharge time in second, and ΔU is the voltage window from the end of the IR drop to the end of the discharge process in Volts.

Acknowledgment

We gratefully acknowledge the financial support of the National Basic Research Program of China (2009CB226102).

Notes and references

[a] *State Key Laboratory of Catalysis, Dalian Institute of Chemical Physics, Chinese Academy of Science, PO Box 110, Dalian,116023, P. R. China. E-mail: taozhang@dicp.ac.cn. Fax:+86-411-84691570; Tel:+86-411-84379015;*

[b] *Beijing Key Laboratory of Green Chemical Reaction Engineering and Technology, Department of Chemical Engineering, Tsinghua University, Beijing 100084, P. R. China*

[c] *Shenyang National Laboratory for Materials Science Institute of Metal Research, Chinese Academy of Sciences, 72 Wenhua Road, Shenyang 110016, P. R. China. E-mail: dssu@imr.ac.cn*

[d] *Key Laboratory of Carbon Materials, Institute of Coal Chemistry, Chinese Academy of Sciences, Taoyuan South Road 27, Taiyuan 030001, P.R. China*

[e] *Graduate University of Chinese Academy of Science, Beijing 100049, P. R. China.*

† Electronic Supplementary Information (ESI) available: Proposed synthesis scheme, XPS, and TEM images of Bx-OMC. See DOI: 10.1039/b000000x/

1. D. S. Su and R. Schlögl, *ChemSusChem*, 2010, **3**, 136; R. Liu, J. Duay and S. B. Lee, *Chem. Commun.*, 2011, **47**, 1384.
2. C. D. Liang, Z. J. Li and S. Dai, *Angew. Chem. Int. Ed.*, 2008, **47**, 3696; Y. F. Shi, Y. Wan and D. Y. Zhao, *ChemSocRev*, 2011, **40**, 3854.
3. Y. H. Zhang, A. Q. Wang and T. Zhang, *Chem. Commun.*, 2010, **46**, 862; J. M. Xu, A. Q. Wang, X. D. Wang, D. S. Su and T. Zhang, *Nano Res.*, 2011, **4**, 50; Z. X. Wu and D. Y. Zhao, *Chem. Commun.*, 2011, **47**, 3332.
4. S. Shiraishi, M. Kibe, T. Yokoyama, H. Kurihara, N. Patel, A. Oya, Y. Kaburagi and Y. Hishiyama, *Appl. Phys. A*, 2006, **82**, 585; D. Portehault, C. Giordano, C. Gervais, I. Senkovska, S. Kaskel, C. Sanchez and M. Antonietti, *Adv. Funct. Mater.*, 2010, **20**, 1827; Y. Wang, J. S. Zhang, X. C. Wang, M. Antonietti and H. R. Li, *Angew. Chem. Int. Ed.*, 2010, **49**, 3356; S. L. Ding, S. J. Zheng, M. J. Xie, L. M. Peng, X. F. Guo and W. P. Ding, *Micropor. Mesopor. Mat.*, 2011, **142**, 609.
5. D. W. Wang, F. Li, Z. G. Chen, G. Q. Lu and H. M. Cheng, *Chem. Mater.*, 2008, **20**, 7195; X. Zhai, Y. Song, L. Zhi, J. Shi and Q, Guo, *New Carbon Mater.*, 2011, **26**, 211-216; Z. L. Zhai, Y. Song, J. Q. Liu, P. Li, M. Zhong, C. Ma, H. Q. Wang, Q. G. Guo and L. J. Zhi, *J. Electrochem. Soc.*, 2012, **159**, E177.
6. T. Kwon, H. Nishihara, H. Itoi, Q. H. Yang and T. Kyotani, *Langmuir*, 2009, **25**, 11961; P. F. Fulvio, J. S. Lee, R. T. Mayes, X. Q. Wang, S. M. Mahurin and S. Dai, *Phys. Chem. Chem. Phys.*, 2011, **13**, 13486
7. .X. C. Zhao, A. Q. Wang, J. W. Yan, G. Q. Sun, L. X. Sun and T. Zhang, *Chem. Mater.*, 2010, **22**, 5463; X. C. Zhao, Q. Zhang, B. S. Zhang, C. M.Chen, A. Q. Wang, T. Zhang and D. S. Su, *J. Mater. Chem.*, 2012, **22**, 4963.
8. C. Moreno-Castilla, M. B. Dawidziuk, F. Carrasco-Marin and Z. Zapata-Benabithe, *Carbon*, 2011, **49**, 3808.
9. P. Mohanty and K. Landskron, *J. Mater. Chem.*, 2009, **19**, 2400.
10. .S. H. Liu, M. T. Wu, Y. H. Lai, C. C. Chiang, N. Y. Yu and S. B. Liu, *J. Mater. Chem.*, 2011, **21**, 12489; X. Jin, V. V. Balasubramanian, S. T. Selvan, D. P. Sawant, M. A. Chari, G. Q. Lu and A. Vinu, *Angew. Chem. Int. Ed.*, 2009, **48**, 7884
11. J. Zhang, X. Liu, R. Blume, A. H. Zhang, R. Schlogl and D. S. Su, *Science*, 2008, **322**, 73

12. G. Hasegawa, M. Aoki, K. Kanamori, K. Nakanishi, T. Hanada and K. Tadanaga, *J. Mater. Chem.*, 2011, **21**, 2060.
13. L. Peng, A. Philippaerts, X. X. Ke, J. Van Noyen, F. De Clippel, G. Van Tendeloo, P. A. Jacobs and B. F. Sels, *Catal. Today*, 2010, **150**, 140.
14. T. Morita and N. Takami, *Electrochim. Acta*, 2004, **49**, 2591.
15. D. S. Su, J. J. Delgado, X. Liu, D. Wang, R. Schlogl, L. F. Wang, Z. Zhang, Z. C. Shan and F. S. Xiao, *Chem. Asian J.*, 2009, **4**, 1108; L. Liu, Q. F. Deng, B. Agula, X. Zhao, T. Z. Ren and Z. Y. Yuan, *Chem. Commun.*, 2011, **47**, 8334.
16. L. R. Radovic, M. Karra, K. Skokova and P. A. Thrower, *Carbon*, 1998, **36**, 1841.
17. Y. H. Deng, Y. Cai, Z. K. Sun, D. Gu, J. Wei, W. Li, X. H. Guo, J. P. Yang and D. Y. Zhao, *Adv. Funct. Mater.*, 2010, **20**, 3658; C. H. Huang, Q. Zhang, T. C. Chou, C. M. Chen, D. S. Su and R. A. Doong, *ChemSusChem*, 2012, **5**, 563.
18. S. J.A., M. P.C. and S. W.E., *J. Catal.*, 1980, **65**, 195.
19. C. Martin, G. Lligadas, J. C. Ronda, M. Galia and V. Cadiz, *J. Polym. Sci. Pol. Chem*, 2006, 44, 6332; Y. J. Lee and H. Hatori, *Mater. Chem. Phys.*, 2003, **82**, 258.
20. I. D. Brown and R. D. Shannon, *Acta Cryst.*, 1973, **A29**, 266.
21. Y. P. Zhai, Y. Q. Dou, D. Y. Zhao, P. F. Fulvio, R. T. Mayes and S. Dai, *Adv. Mater.*, 2011, **23**, 4828; C. M. Chen, Q. Zhang, X. C. Zhao, B. S. Zhang, Q. Q. Kong, M. G. Yang, Q. H. Yang, M. Z. Wang, Y. G. Yang, R. Schlogl and D. S. Su, *J. Mater. Chem.*, 2012, **22**, 14076; G. H. Xu, C. Zheng, Q. Zhang, J. Q. Huang, M. Q. Zhao, J. Q. Nie, X. H. Wang and F. Wei, *Nano Res.*, 2011, **4**, 870.
22. C. T. Hsieh and H. Teng, *Carbon*, 2002, **40**, 667-674.
23. X. X. Wu and L. R. Radovic, *Carbon*, 2005, **43**, 1768.
24. D. Hulicova-Jurcakova, A. M. Puziy, O. I. Poddubnaya, F. Suarez-Garcia, J. M. D. Tascon and G. Q. Lu, *J. Am. Chem. Soc.*, 2009, **131**, 5026.